



Experimental Demonstration of Memory-Enhanced Quantum Communication

Citation

Bhaskar, M K, Riedinger, R, Machielse, B, Levonian, D S, Nguyen, C T, Knall, E N, Park, H, Englund, D, Lončar, M, Sukachev, D D, and Lukin, M D. "Experimental Demonstration of Memory-enhanced Quantum Communication." Nature (London) 580, no. 7801 (2020): 60-64.

Permanent link

<https://nrs.harvard.edu/URN-3:HUL.INSTREPOS:37367189>

Terms of Use

This article was downloaded from Harvard University's DASH repository, and is made available under the terms and conditions applicable to Other Posted Material, as set forth at <http://nrs.harvard.edu/urn-3:HUL.InstRepos:dash.current.terms-of-use#LAA>

Share Your Story

The Harvard community has made this article openly available.
Please share how this access benefits you. [Submit a story](#).

[Accessibility](#)

Experimental demonstration of memory-enhanced quantum communication

M. K. Bhaskar^{1,*}, R. Riedinger^{1,*}, B. Machielse^{1,*}, D. S. Levonian^{1,*}, C. T. Nguyen^{1,*},
E. N. Knall², H. Park^{1,3}, D. Englund⁴, M. Lončar², D. D. Sukachev¹, M. D. Lukin^{1,†}

¹*Department of Physics, Harvard University, Cambridge, MA 02138, USA*

²*John A. Paulson School of Engineering and Applied Sciences, Harvard University, Cambridge, MA 02138, USA*

³*Department of Chemistry and Chemical Biology, Harvard University, Cambridge, MA 02138, USA*

⁴*Research Laboratory of Electronics, MIT, Cambridge, MA 02139, USA*

The ability to communicate quantum information over long distances is of central importance in quantum science and engineering¹. While some applications of quantum communication such as secure quantum key distribution (QKD)^{2,3} are already being successfully deployed⁴⁻⁷, their range is currently limited by photon losses and cannot be extended using straightforward measure-and-repeat strategies without compromising unconditional security⁸. Alternatively, quantum repeaters⁹, which utilize intermediate quantum memory nodes and error correction techniques, can extend the range of quantum channels. However, their implementation remains an outstanding challenge¹⁰⁻¹⁶, requiring a combination of efficient and high-fidelity quantum memories, gate operations, and measurements. Here we use a single solid-state spin memory integrated in a nanophotonic diamond resonator¹⁷⁻¹⁹ to

21 **implement asynchronous photonic Bell-state measurements, a key component of quantum**
22 **repeaters. In a proof-of-principle experiment, we demonstrate high-fidelity operation that**
23 **effectively enables quantum communication at a rate that surpasses the ideal loss-equivalent**
24 **direct-transmission method while operating at megahertz clock speeds. These results repre-**
25 **sent a significant step towards practical quantum repeaters and large-scale quantum networks^{2,20}.**

26 Efficient, long-lived quantum memory nodes are expected to play an essential role in extend-
27 ing the range of quantum communication⁹, as they enable asynchronous quantum logic operations,
28 such as Bell-state measurements (BSM), between optical photons. Such an asynchronous BSM is
29 central to many quantum communication protocols, including the realization of scalable quantum
30 repeaters⁹ with multiple intermediate nodes. Its elementary operation can be understood by con-
31 sidering a specific implementation of quantum cryptography^{21,22} illustrated in Fig. 1a. Here two
32 remote communicating parties, Alice and Bob, try to agree on a key that is secure against potential
33 eavesdroppers. They each send a randomly chosen photonic qubit $\{|\pm x\rangle, |\pm y\rangle\}$ encoded in one
34 of two conjugate bases (X or Y) across a lossy channel to an untrusted central node (Charlie),
35 who performs a BSM and reports the result over an authenticated public channel. After a number
36 of iterations, Alice and Bob publicly reveal their choice of bases to obtain a correlated bit string
37 (sifted key) from the cases when they used a compatible basis. A potentially secure key can sub-
38 sequently be distilled provided the BSM error rate is low enough. While a photonic BSM can be
39 implemented with linear optics and single photon detectors, in this “direct-transmission” approach,
40 the BSM is only successful when photons from Alice and Bob arrive simultaneously. Thus, when
41 Alice and Bob are separated by a lossy fiber with a total transmission probability $p_{A \rightarrow B} \ll 1$, Char-

42 lie measures photon coincidences with probability also limited by $p_{A \rightarrow B}$, leading to a fundamental
43 bound⁸ on the maximum possible distilled key rate of $R_{\max} = p_{A \rightarrow B}/2$ bits per channel use for an
44 unbiased basis choice⁴. While linear optical techniques to circumvent this bound are now being
45 actively explored²³, they offer only limited improvement and cannot be scaled beyond a single
46 intermediate node. Alternatively, this bound can be surpassed using a quantum memory node at
47 Charlie's location. In this approach, illustrated in Fig. 1b, the state of Alice's photon is stored in
48 the heralded memory while awaiting receipt of Bob's photon over the lossy channel. Once the
49 second photon arrives, a BSM between Alice's and Bob's qubits yields a distilled key rate that for
50 an ideal memory scales as²⁴ $R_s \propto \sqrt{p_{A \rightarrow B}}$, potentially leading to substantial improvement over
51 direct transmission.

52 This Letter describes the operation of a quantum node that enables BSM rates that exceed
53 those of an ideal system based on linear optics. We focus on the demonstration and characterization
54 of the BSM node, leaving the implementation of source-specific technical components of full-scale
55 QKD systems, such as decoy states²⁵, basis biasing²⁶, a finite key error analysis²⁷, and a physical
56 separation of Alice and Bob for future work. Our realization is based on a single silicon-vacancy
57 (SiV) color-center integrated inside a diamond nanophotonic cavity¹⁷⁻¹⁹ (Fig. 2a). Its key figure-
58 of-merit, the cooperativity¹³ C , describes the ratio of the interaction rate with individual cavity
59 photons compared to all dissipation rates. A low mode volume ($0.5(\lambda/n)^3$), high quality factor
60 (2×10^4), and nanoscale positioning of SiV centers enable an exceptional $C = 105 \pm 11$. Cavity
61 photons at 737 nm are critically coupled to a waveguide and adiabatically transferred into a single-
62 mode optical fiber¹⁸ that is routed to superconducting nanowire single-photon detectors, yielding

63 a full system detection efficiency of about 85% (Methods). The device is placed inside a dilution
64 refrigerator, resulting in electronic spin quantum memory¹⁹ time $T_2 > 0.2$ ms at temperatures
65 below 300 mK.

66 The operating principle of the SiV-cavity based spin-photon interface is illustrated in Fig. 2.
67 Spin dependent modulation of the cavity reflection at incident probe frequency f_0 (Fig. 2b) results
68 in the direct observation of electron spin quantum jumps (Fig. 2c, inset), enabling nondestructive
69 single-shot readout of the spin state (Fig. 2c) in 30 μ s with fidelity $F = 0.9998^{+0.0002}_{-0.0003}$. Coherent
70 control of the SiV spin qubit ($f_Q \approx 12$ GHz) is accomplished using microwave fields delivered via
71 an on-chip gold coplanar waveguide¹⁹. We utilize both optical readout and microwave control to
72 perform projective feedback-based initialization of the SiV spin into the $|\downarrow\rangle$ state with a fidelity
73 of $F = 0.998 \pm 0.001$. Spin-dependent cavity reflection also enables quantum logic operations
74 between an incoming photonic time-bin qubit, defined by a phase-coherent pair of attenuated laser
75 pulses, and the spin memory^{19,28}. We characterize this by using the protocol illustrated in Fig. 2d
76 to generate the spin-photon entangled state $(|e \uparrow\rangle + |l \downarrow\rangle)/\sqrt{2}$ conditioned on successful reflection
77 of an incoming single photon with overall heralding efficiency $\eta = 0.423 \pm 0.004$ (Methods).
78 Here, $|e\rangle$ and $|l\rangle$ denote the presence of a photon in an early or late time-bin separated by $\delta t =$
79 142 ns respectively. We characterize the entangled state by performing measurements in the joint
80 spin-photon ZZ and XX bases (Fig. 2e), implementing local operations on the reflected photonic
81 qubit with a time-delay interferometer (Fig. 2a, dashed box). By lowering the average number of
82 photons $\langle n \rangle_m$ incident on the device during the SiV memory time, we reduce the possibility that
83 an additional photon reaches the cavity without being subsequently detected, enabling high spin-

84 photon gate fidelities for small $\langle n \rangle_m$ (Fig. 2f). For $\langle n \rangle_m = 0.002$ we measure a lower bound on the
 85 fidelity¹⁹ of the spin-photon entangled state of $F \geq 0.944 \pm 0.008$, primarily limited by residual
 86 reflections from the $|\downarrow\rangle$ state.

87 This spin-photon logic gate can be directly used to herald the storage of an incoming pho-
 88 tonic qubit by interferometrically measuring the reflected photon in the X basis¹⁹. To implement
 89 a memory-assisted BSM, we extend this protocol to accommodate a total of N photonic qubit
 90 time-bins within a single initialization of the memory (Fig. 3a). Each individual time-bin qubit
 91 is encoded in the relative amplitudes and phases of a pair of neighboring pulses separated by δt .
 92 Detection of a reflected photon heralds the arrival of the photonic qubit formed by the two inter-
 93 fering pulses without revealing its state¹⁹. Two such heralding events, combined with subsequent
 94 spin-state readout in the X basis, constitute a successful BSM on the incident photons. This can
 95 be understood without loss of generality by restricting input photonic states to be encoded in the
 96 relative phase ϕ between neighboring pulses with equal amplitude: $(|e\rangle + e^{i\phi}|l\rangle)/\sqrt{2}$ (Fig. 3b).
 97 Detection of the first reflected photon in the X basis teleports its quantum state onto the spin, result-
 98 ing in the state $(|\uparrow\rangle + m_1 e^{i\phi_1} |\downarrow\rangle)/\sqrt{2}$, where $m_1 = \pm 1$ depending on which detector registers the
 99 photon¹⁹. Detection of a second photon at a later time within the electron spin T_2 results in the spin
 100 state $(|\uparrow\rangle + m_1 m_2 e^{i(\phi_1 + \phi_2)} |\downarrow\rangle)/\sqrt{2}$. The phase of this spin state depends only on the sum of the
 101 incoming phases and the product of their detection outcomes, but not the individual phases them-
 102 selves. As a result, if the photons were sent with phases that meet the condition $\phi_1 + \phi_2 \in \{0, \pi\}$,
 103 a final measurement of the spin in the X basis ($m_3 = \pm 1$) completes an asynchronous BSM,
 104 distinguishing two of the four Bell-states based on the total parity $m_1 m_2 m_3 = \pm 1$ (Methods).

105 This approach can be directly applied to generate a correlated bit-string within the protocol
 106 illustrated in Fig. 1a. We analyze the system performance by characterizing the overall quantum-bit
 107 error rate (QBER)^{4,21} for $N = 124$ photonic qubits per memory initialization. We use several ran-
 108 dom bit strings of incoming photons from $\{|\pm x\rangle, |\pm y\rangle\}$ and observe strong correlations between
 109 the resulting BSM outcome and the initial combination of input qubits for both bases (Fig. 3c).
 110 Using this method, we estimate the average QBER to be $E = 0.116 \pm 0.002$ for all combinations
 111 of random bit strings measured, significantly below the limit of $E_i = 0.146$, which could provide
 112 security against individual attacks⁴ (note that the measured error rate is also well below the min-
 113 imum average QBER²¹ of $E_{lo} = 0.125$ achievable using a linear optics BSM with weak coherent
 114 pulse inputs, see Methods). In our experiment, the QBER is affected by technical imperfections in
 115 the preparation of random strings of photonic qubits. We find specific periodic patterns of photonic
 116 qubits to be less prone to these effects, resulting in a QBER as low as $E = 0.097 \pm 0.006$, which
 117 falls within the threshold corresponding to unconditional security³ of $E_u = 0.110$ with a confi-
 118 dence level of 0.986 (Methods). We further verify security by testing the Bell-CHSH inequality¹⁴
 119 using input states from four different bases, each separated by an angle of 45° (Methods). We find
 120 that the correlations between input photons (Fig. 3d) violate the Bell-CHSH inequality $S_\pm \leq 2$,
 121 observing $S_+ = 2.21 \pm 0.04$ and $S_- = 2.19 \pm 0.04$ for positive and negative BSM parity results
 122 respectively. This result demonstrates that this device can be used for quantum communication
 123 that is secured by Bell's theorem.

124 Finally, we benchmark the performance of memory-assisted quantum communication. For
 125 each experiment, we model an effective channel loss by considering the mean photon number $\langle n \rangle_p$

126 incident on the device per photonic qubit. Assuming that Alice and Bob emit roughly one photon
 127 per qubit, this yields an effective channel transmission probability $p_{A \rightarrow B} = \langle n \rangle_p^2$, resulting in the
 128 maximal distilled key rate R_{\max} per channel use for the direct transmission approach²¹, given by
 129 the red line in Fig. 4. We emphasize that this is a theoretical upper bound for a linear optics
 130 based BSM, assuming ideal single-photon sources and detectors and balanced basis choices. The
 131 measured sifted key rates of the memory-based device are plotted as open circles in Fig. 4. Due to
 132 the high overall heralding efficiency and the large number of photonic qubits per memory time (up
 133 to $N = 504$), the memory-assisted sifted key rate exceeds the capability of a linear-optics based
 134 BSM device by a factor of 78.4 ± 0.7 at an effective channel loss of about 88 dB.

135 In practice, errors introduced by the quantum memory node could leak information to the en-
 136 vironment, reducing the quality and potential security of the sifted key³. A shorter secure key can
 137 be recovered from a sifted key with finite QBER using classical error correction and privacy am-
 138 plification techniques. The fraction of distilled bits r_s that can be secure against individual attacks
 139 rapidly diminishes⁴ as the QBER approaches $E_i = 0.147$. For each value of the effective channel
 140 loss, we estimate the QBER and use it to compute r_s , enabling extraction of distilled key rates R_S ,
 141 plotted in black in Fig. 4. Even after error-correction, we find that the memory-assisted distilled
 142 key rate outperforms the ideal limit for the corresponding direct-transmission implementation by a
 143 factor of up to $R_S/R_{\max} = 4.1 \pm 0.5$ (± 0.1 systematic uncertainty, for $N = 124$). We further find
 144 that this rate also exceeds the fundamental bound on repeaterless communication⁸ $R_S \leq 1.44p_{A \rightarrow B}$
 145 with a statistical confidence level of 99.2% ($+0.2\%$ -0.3% systematic uncertainty, see Methods). Despite
 146 experimental overhead time associated with operating the device (T_R in Fig. 1b), the performance

147 of the memory-assisted BSM node (for $N = 248$) is competitive with an ideal unassisted system
148 running at a 4 MHz average clock rate (Methods).

149 These experiments demonstrate a form of quantum advantage allowed by memory-based
150 communication nodes and represent a crucial step towards realizing functional quantum repeaters.
151 Several important technical improvements will be necessary to apply this advance for practical
152 long-distance quantum communication. First, this protocol must be implemented using truly inde-
153 pendent, distant communicating parties. Additionally, frequency conversion from telecommunica-
154 tions wavelengths to 737 nm, as well as low-loss optical elements used for routing photons to and
155 from the memory node, will need to be incorporated. Finally, rapid generation of provably secure
156 keys will require implementation of decoy-state protocols²⁵, biased bases²⁶, and finite-key error
157 analyses²⁷, all compatible with the present approach. With these improvements, our approach is
158 well-suited for deployment in real-world settings. It does not require phase stabilization of long-
159 distance links and operates efficiently in the relevant regime of $p_{A \rightarrow B} \approx 70$ dB, corresponding to
160 about 350 km of telecommunications fiber. Additionally, a single device can be used at the center
161 of a star network topology²⁹, enabling quantum communication between several parties beyond the
162 metropolitan scale. Furthermore, the present approach can be extended along several directions.
163 The use of long-lived ^{13}C nuclear spin qubits could eliminate the need to operate at low total $\langle n \rangle_m$
164 and would provide longer storage times, potentially enabling hundred-fold enhancement of BSM
165 success rates^{15,19}. Recently implemented strain-tuning capabilities³⁰ should allow for operation of
166 many quantum nodes at a common network frequency. Unlike linear-optics based alternatives²³,
167 the approach presented here can be extended to implement the full repeater protocol, enabling a

168 polynomial scaling of the communication rate with distance⁹. Finally, the demonstrated multi-
169 photon gate operations can also be adapted to engineer large cluster-states of entangled photons³¹,
170 which can be utilized for rapid quantum communication³². Implementation of these techniques
171 could enable the realization and applications of scalable quantum networks¹ beyond QKD, rang-
172 ing from non-local quantum metrology⁷ to modular quantum computing architectures²⁰.

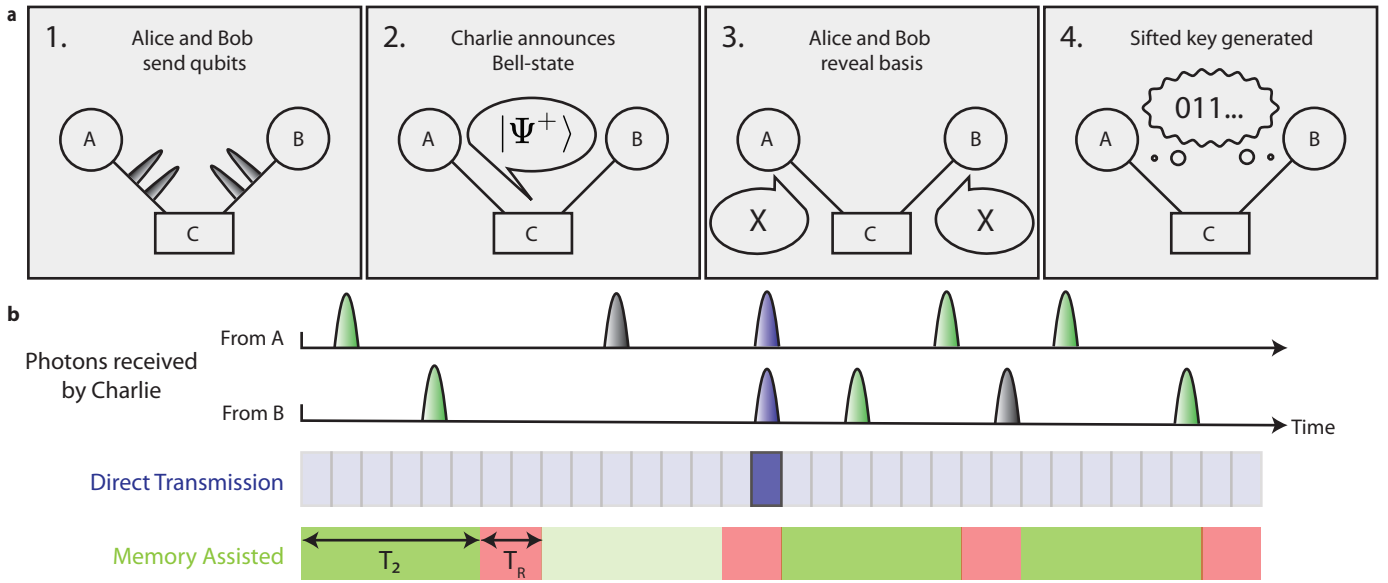


Figure 1: Concept of memory-enhanced quantum communication. **a**, Quantum communication protocol. Alice and Bob send qubits encoded in photons to a measurement device (Charlie) in between them. Charlie performs a BSM and announces the result. After verifying which rounds Alice and Bob sent qubits in compatible bases, a sifted key is generated. **b**, Illustration of memory-enhanced protocol. Photons arrive at Charlie from A and B at random times over a lossy channel, and are unlikely to arrive simultaneously (indicated in purple), leading to a low BSM success rate for direct transmission. Despite overhead time T_R associated with operating a quantum memory (red), a BSM can be performed between photons that arrive at Charlie within memory coherence time T_2 , leading to higher success rates (green). BSM successes and failures are denoted by dark and light shaded windows respectively for both approaches.

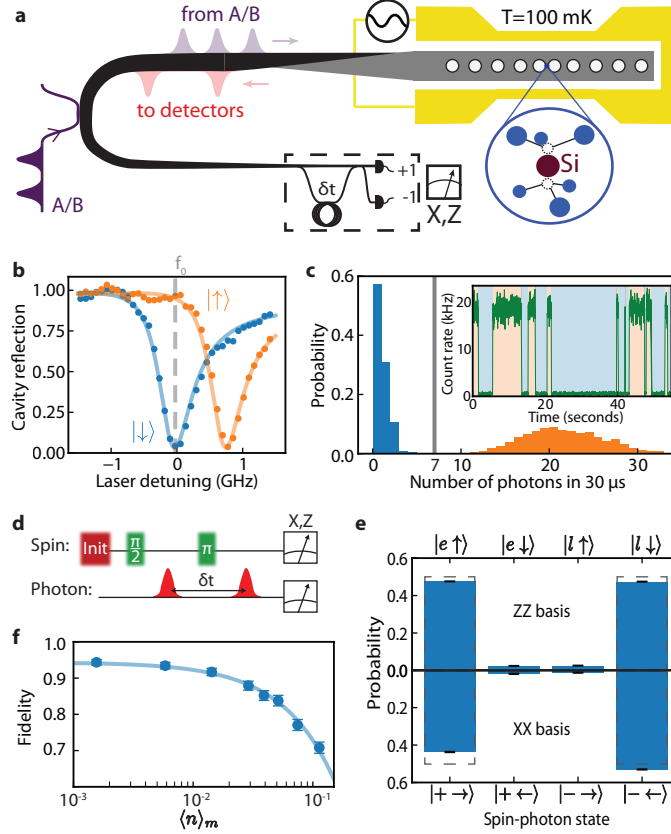


Figure 2: Realization of heralded spin-photon gate. **a**, Schematic of memory-assisted implementation of Charlie’s measurement device. Weak pulses derived from a single laser simulate incoming photons from Alice and Bob (purple). Reflected photons (red) are detected in a heralding setup (dashed box). **b**, Reflection spectrum of memory node, showing spin-dependent device reflectivity. **c**, Histogram of detected photon numbers during a $30\ \mu\text{s}$ laser pulse, enabling single-shot readout based on a threshold of 7 photons. (Inset) Electron spin quantum jumps under weak illumination. **d**, Schematic of spin-photon quantum logic operation used to generate and verify spin-photon entangled state. **e**, Characterization of resulting spin-photon correlations in the ZZ and XX bases. Dashed bars show ideal values. **f**, Measured spin-photon entanglement fidelity as a function of $\langle n \rangle_m$, the average incident photon number during each initialization of the memory.

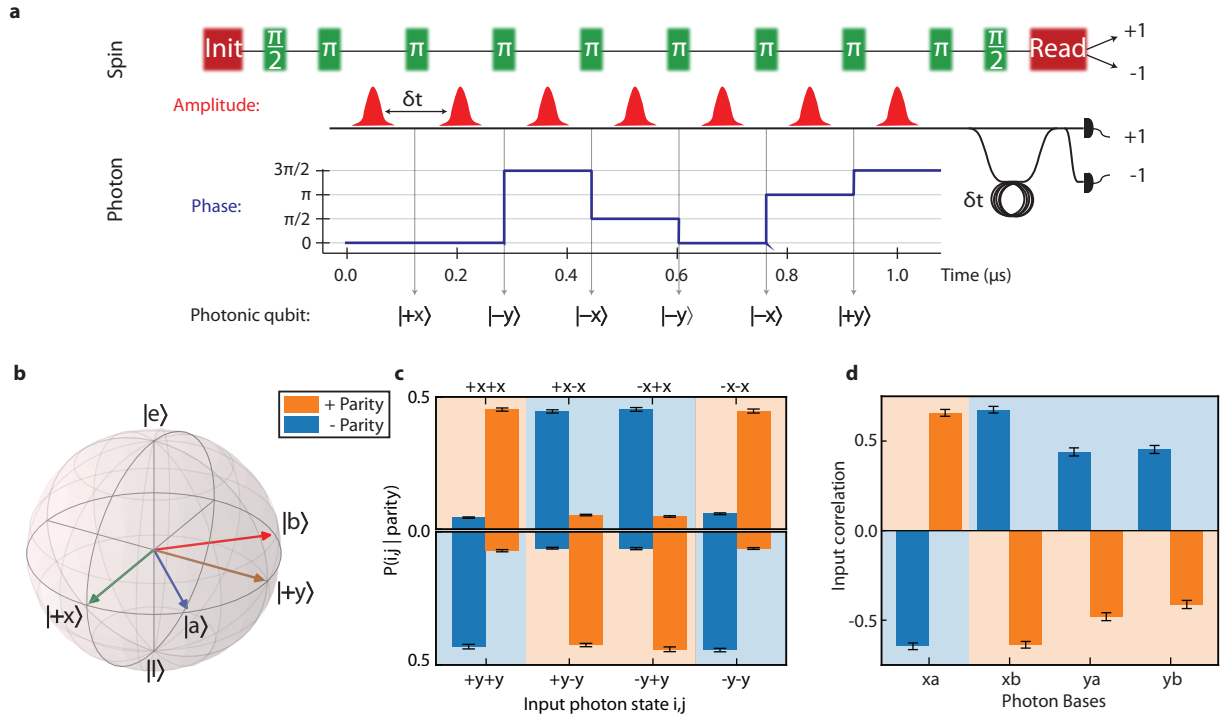


Figure 3: Asynchronous Bell-state measurements using quantum memory. **a**, Example sequence with $N = 6$ photonic qubits sent in a single memory time. Microwave π pulses (green) are interleaved with incoming optical pulses. Photons have fixed amplitude (red) and qubits are defined by the relative phases between subsequent pulses (blue). **b**, Bloch sphere representation of input photonic time-bin qubits used for characterization. **c**, Characterization of asynchronous BSM. Conditional probabilities for Alice and Bob to have sent input states (i, j) given a particular parity outcome for input states in the X (top) and Y (bottom) bases. **d**, Bell test using the CHSH inequality. Conditioned on the BSM outcome, the average correlation between input photons is plotted for each pair of bases used (Methods). Shaded backgrounds denote the expected parity.

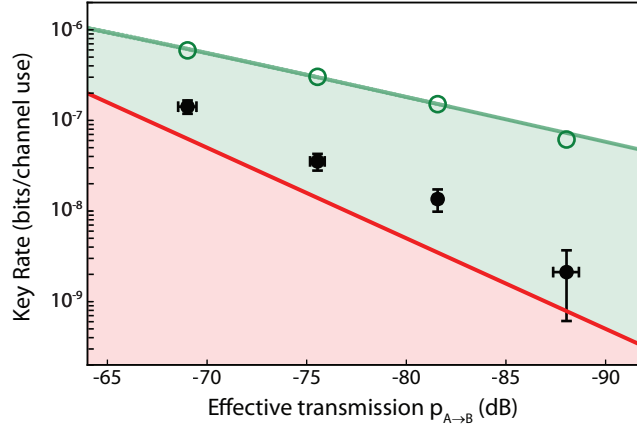


Figure 4: Performance of memory-assisted quantum communication. Log-log plot of key rate in bits per channel use versus effective channel transmission ($p_{A \rightarrow B} = \langle n \rangle_p^2$, where $\langle n \rangle_p$ is the average number of photons incident on the measurement device per photonic qubit). Red line: theoretical maximum for loss-equivalent direct transmission experiment. Green open circles: experimentally measured sifted key rate (green line is the expected rate). To ensure optimal operation of the memory, $\langle n \rangle_m = \langle n \rangle_p N \approx 0.02$ is kept constant (Methods). From left to right, points correspond to $N = \{60, 124, 248, 504\}$. Black filled circles: distilled key rates R_S using memory device. Vertical error bars are given by the 68% confidence interval and horizontal error bars represent the standard deviation of the systematic power fluctuations.

173 **Methods**

174 Experimental setup and device fabrication^{18,30,33,34} for millikelvin nanophotonic cavity QED ex-
175 periments with SiV centers are thoroughly described in a separate publication³⁵. Measurements of
176 the cavity QED parameters of the device used in the main text (Extended Data Fig. 1), microwave
177 characterization of the spin qubit (Extended Data Fig. 2), and statistical techniques for estimating
178 QBER are described in detail the Supplementary Methods.

179 **Experimental details.** An asynchronous BSM (Fig. 3a) relies on (1) precise timing of the ar-
180 rival of optical pulses (corresponding to photonic qubits^{36,37} from Alice and Bob) with microwave
181 control pulses on the quantum memory and (2) interferometrically stable rotations on reflected
182 time-bin qubits for successful heralding. In order to accomplish (1), all equipment used for gen-
183 eration of microwave and optical fields is synchronized by a single device (National Instruments
184 HSDIO, Extended Data Fig. 1a) with programming described in Extended Data Table 1-2.

185 In order to accomplish (2), we use a single, narrow linewidth (< 50 kHz) Ti:Sapphire laser
186 (M Squared SolsTiS-2000-PSX-XF, Extended Data Fig. 1b) both for generating photonic qubits
187 and locking the time-delay interferometer (TDI) used to herald their arrival. In the experiment,
188 photonic qubits are reflected from the device, sent into the TDI, and detected on superconducting
189 nanowire single photon detectors (SNSPD, Photon Spot). All detected photons are processed dig-
190 itally on a field-programmable gate array (FPGA, Extended Data Fig. 1a), and the arrival times of
191 these heralding signals are recorded on a time-tagger (TT, Extended Data Fig. 1a), and constitute
192 one bit of information of the BSM (m_1 or m_2). At the end of the experiment, a $30 \mu\text{s}$ pulse from

193 the readout path is reflected off the device, and photons are counted in order to determine the spin
194 state (m_3) depending on the threshold shown in Fig. 2c.

195 To minimize thermal drift of the TDI, it is mounted to a thermally weighted aluminum bread-
196 board, placed in a polyurethane foam-lined and sand filled briefcase, and secured with glue to
197 ensure passive stability on the minute timescale. We halt the experiment and actively lock the in-
198 terferometer to the sensitive Y-quadrature every ~ 200 ms by changing the length of the roughly
199 28 m long (142 ns) delay line with a cylindrical piezo. In order to use the TDI for X-measurements
200 of the reflected qubits, we apply a frequency shift of 1.8 MHz using the qubit AOM, which is 1/4
201 of the free-spectral range of the TDI. Since the nanophotonic cavity, the TDI, and the SNSPDs are
202 all polarization sensitive, we use various fiber-based polarization controllers (Extended Data Fig.
203 1b). All fibers in the network are covered with aluminum foil to prevent thermal polarization drifts.
204 This results in an interference visibility of the TDI of $> 99\%$ that is stable for several days without
205 any intervention with lab temperature and humidity variations of $\pm 1^\circ$ C and $\pm 5\%$ respectively.

206 In order to achieve high-fidelity operations we have to ensure that the laser frequency (which
207 is not locked) is resonant with the SiV frequency f_0 (which is subject to the spectral diffusion³⁵).
208 To do that we implement a so-called preselection procedure, described in Extended Data Table
209 1-2 and Extended Data Fig. 1a. First, the SiV spin state is initialized by performing a projective
210 measurement and applying microwave feedback. During each projective readout, the reflected
211 counts are compared with two thresholds: a “readout” threshold of 7 photons (used only to record
212 m_3), and a “status” threshold of 3 photons. The status trigger is used to prevent the experiment
213 from running in cases when the laser is no longer on resonance with f_0 , or if the SiV has ionized to

214 an optically inactive charge state. The duty cycle of the status trigger is externally monitored and
215 is used to temporarily abort the experiment and run an automated re-lock procedure that locates
216 and sets the laser to the new frequency f_0 , reinitializing the SiV charge state with a 520 nm laser
217 pulse if necessary. This protocol enables fully automated operation at high fidelities (low QBER)
218 for several days without human intervention.

219 **Fiber network.** The schematic of the fiber-network used to deliver optical pulses to and collect
220 reflected photons from the nanophotonic memory device is shown in Extended Data Fig. 1b. Pho-
221 tons are routed through the lossy (1%) port of a 99:1 fiber beamsplitter (FBS) to the nanophotonic
222 device. We note that for practical implementation of memory-assisted quantum communication,
223 an efficient optical switch or circulator should be used instead. In this experiment, since we focus
224 on benchmarking the performance of the memory device itself, the loss introduced by this beam-
225 splitter is incorporated into the estimated channel loss. Reflected photons are collected and routed
226 back through the efficient (99%) port of the FBS and are sent to the TDI in the heralding setup.

227 The outputs of the TDI are sent back into the dilution refrigerator and directly coupled to
228 SNSPDs (PhotonSpot), which are mounted at the 1K stage and are coated with dielectrics to op-
229 timize detection efficiency exactly at 737 nm. We estimate all losses that reduce the heralding ef-
230 ficiency η by two independent calibration methods. These rely on three calibrated photodetectors
231 shown in Extended Data Fig. 1b (M1, M2, MC) and are described in detail in the Supplemen-
232 tary Methods, yielding consistent values of $\eta_1 = 0.425 \pm 0.008$ and $\eta_2 = 0.422 \pm 0.005$. This
233 corresponds to a collection efficiency of reflected photons of $\approx 85\%$.

234 For values cited in the main text and data points presented in the figures, we use an average
 235 value of the heralding efficiency inferred from the two calibration techniques: $\eta = 0.423 \pm 0.004$.
 236 The residual uncertainty in the heralding efficiency results in a systematic uncertainty, which is
 237 explicitly mentioned in the main text where appropriate. We note that this heralding efficiency is
 238 consistent with the scaling of spin decoherence with the number of photons at the cavity $\langle n \rangle_m$. An
 239 example of this effect is shown in the red point in Extended Data Fig. 3e.

240 **Theoretical description of asynchronous Bell state measurement.** Due to the critical coupling
 241 of the nanocavity, the memory node only reflects photons when the SiV spin is in the state $|\uparrow\rangle$.
 242 The resulting correlations between the spin and the reflected photons can still be used to realize
 243 a BSM between two asynchronously arriving photonic time-bin qubits using an adaptation of the
 244 well known proposal of Duan and Kimble²⁸ for entangling a pair of photons incident on an atom-
 245 cavity system. As a result of the critical coupling, we only have access to two of the four Bell
 246 states at any time, with the inaccessible Bell states corresponding to photons being transmitted
 247 through the cavity (and thus lost from the detection path). Depending on whether there was an
 248 even or odd number of π -pulses on the spin between the arrival of the two heralded photons, we
 249 distinguish either the $\{|\Phi_{\pm}\rangle\}$ or $\{|\Psi_{\pm}\rangle\}$ states (defined below). For the sake of simplicity, we first
 250 describe the BSM for the case when the early time bin of Alice’s and Bob’s qubits both arrive after
 251 an even number of microwave π pulses after its initialization. Thereafter we generalize this result
 252 and describe the practical consequences for the quantum communication protocol.

253 The sequence begins with a $\pi/2$ microwave pulse, preparing the spin in the state $|\psi_i\rangle =$
 254 $(|\uparrow\rangle + |\downarrow\rangle)/\sqrt{2}$. In the absence of a photon at the device, the subsequent microwave π -pulses,

255 which follow an XY8-N type pattern, decouple the spin from the environment and at the end
 256 of the sequence should preserve the spin state $|\psi_i\rangle$. However, reflection of Alice's photonic qubit
 257 $|A\rangle = (|e\rangle + e^{i\phi_1} |l\rangle)/\sqrt{2}$ from the device results in the entangled spin-photon state $|\psi_A\rangle = (|\uparrow e\rangle +$
 258 $e^{i\phi_1} |\downarrow l\rangle)/\sqrt{2}$. The full system is in the state

$$|\psi_A\rangle = \frac{|+x\rangle (|\uparrow\rangle + e^{i\phi_1} |\downarrow\rangle) + |-x\rangle (|\uparrow\rangle - e^{i\phi_1} |\downarrow\rangle)}{2}. \quad (1)$$

259 Regardless of the input photon state, there is equal probability to measure the reflected photon
 260 to be $|\pm x\rangle$. Thus, measuring the photon in X basis (through the TDI) does not reveal the initial
 261 photon state. After this measurement, the initial state of the photon $|A\rangle$ is teleported onto the spin:
 262 $|\psi_{m_1}\rangle = (|\uparrow\rangle + m_1 e^{i\phi_1} |\downarrow\rangle)\sqrt{2}$, where $m_1 = \pm 1$ denotes the detection outcome of the TDI^{19,38}.
 263 The quantum state of Alice's photon is now stored in the spin state, which is preserved by the
 264 dynamical decoupling sequence.

265 Reflection of the second photon $|B\rangle = (|e\rangle + e^{i\phi_2} |l\rangle)\sqrt{2}$ from Bob results in the spin-photon
 266 state $|\psi_{m_1,B}\rangle = (|\uparrow e\rangle + m_1 e^{i(\phi_1+\phi_2)} |\downarrow l\rangle)/\sqrt{2}$. This state now has a phase that depends on the
 267 initial states of both photons, enabling the photon-photon BSM measurements described below.
 268 Rewriting Bob's reflected photon in the X basis, the full system is in the state

$$|\psi_{m_1,B}\rangle = \frac{|+x\rangle (|\uparrow\rangle + m_1 e^{i(\phi_1+\phi_2)} |\downarrow\rangle) + |-x\rangle (|\uparrow\rangle - m_1 e^{i(\phi_1+\phi_2)} |\downarrow\rangle)}{2}. \quad (2)$$

269 The second measurement result m_2 once again contains no information about the initial state $|B\rangle$,
 270 yet heralds the final spin state $|\psi_{m_1,m_2}\rangle = (|\uparrow\rangle + m_1 m_2 e^{i(\phi_1+\phi_2)} |\downarrow\rangle)$ as described in the main text.
 271 When this state lies along the X axis of the Bloch sphere ($\phi_1 + \phi_2 = \{0, \pi\}$), the final result of the
 272 X basis measurement on the spin state m_3 has a deterministic outcome, dictated by all values of the

273 parameters $\{\phi_1, \phi_2\}$ (known only to Alice and Bob) and $\{m_1, m_2\}$ (which are known to Charlie,
 274 but are completely random). Conversely, all information available to Charlie $\{m_1, m_2, m_3\}$ only
 275 contains information on the correlation between the photonic qubits, not on their individual states.
 276 The resulting truth table for different input states is given in Extended Data Table 3. For all input
 277 states, there is equal probability of measuring ± 1 for each individual measurement m_i . However,
 278 the overall parity of the three measurements $m_1 m_2 m_3$ depends on whether or not the input photons
 279 were the same, or opposite, for inputs $|A\rangle, |B\rangle \in |\pm x\rangle$ or $|\pm y\rangle$.

280 We now address the fact that the BSM distinguishes either between $\{|\Phi_{\pm}\rangle\}$ or $\{|\Psi_{\pm}\rangle\}$ if
 281 there was an even or odd number of microwave π pulses between incoming photons respectively.
 282 This effect arises because each π pulse in the dynamical decoupling sequence toggles an effective
 283 frame change: $Y \leftrightarrow -Y$. The impact on this frame change on the BSM can be seen by writing the
 284 pairs of Bell states ($|\Phi_{\pm}\rangle = (|ee\rangle \pm |ll\rangle)/\sqrt{2}$ and $|\Psi_{\pm}\rangle = (|el\rangle \pm |le\rangle)/\sqrt{2}$) in the X and Y bases,
 285 where we have

$$286 \quad |\Phi_{\pm}\rangle^{(X)} = (|+x\rangle |\pm x\rangle + |\mp x\rangle | -x\rangle)/\sqrt{2} \quad (3)$$

$$287 \quad |\Phi_{\pm}\rangle^{(Y)} = (|+y\rangle |\mp y\rangle + |\pm y\rangle | -y\rangle)/\sqrt{2} \quad (4)$$

$$288 \quad |\Psi_{\pm}\rangle^{(X)} = (|+x\rangle |\pm x\rangle - |\mp x\rangle | -x\rangle)/\sqrt{2} \quad (5)$$

$$|\Psi_{\pm}\rangle^{(Y)} = i(|+y\rangle |\pm y\rangle - |\mp y\rangle | -y\rangle)/\sqrt{2} \quad (6)$$

289 For X basis inputs, as seen by Eq. 3 and 5, switching between $\{|\Phi_{\pm}\rangle\}$ and $\{|\Psi_{\pm}\rangle\}$ measurements
 290 does not affect the inferred correlation between input photons. For Y basis inputs however, this
 291 does result in an effective bit flip in the correlation outcome (see Eq. 4 and 6). In practice, Alice

292 and Bob can keep track of each Y photon sent and apply a bit flip accordingly, as long as they have
293 the appropriate timing information about MW pulses applied by Charlie. If Charlie does not give
294 them the appropriate information, this will result in an increased QBER which can be detected.

295 As an additional remark, this scheme also works for pairs of photons that are not both in
296 the X or Y basis but still satisfy the condition $\phi_1 + \phi_2 = 0$. For example, $|a\rangle$ and $|b\rangle$ from Fig.
297 3b satisfy this condition. In this case, adequate correlations can still be inferred about the input
298 photons, although they were sent in different bases.

299 Finally, we would like to note that this asynchronous scheme for performing a BSM between
300 two pulses has an important advantage over the synchronous, linear-optical implementation. In the
301 case where Alice and Bob use attenuated laser pulses to encode photonic qubits, which is by far
302 the most technologically simple implementation, there is an inherent QBER of 25% for photons
303 sent in the X and Y bases. This is because the linear-optical implementation relies on the pulses to
304 overlap on a beamsplitter and interfere via the Hong-ou-Mandel effect, which has a finite visibility
305 of 50% for coherent pulses²¹. Intuitively, this finite error arises from a fundamental inability to
306 distinguish between detection outcomes where two individual single-photons arrived from Alice
307 and Bob versus a two-photon component from either Alice or Bob in the synchronous scheme. In
308 the asynchronous scheme, since pulses do not arrive at the same time from Alice and Bob, this
309 error is mitigated. As a result, for ideal quantum memory operation and sufficiently attenuated
310 laser pulses, the ultimate limit to the QBER is zero.

311 **Test of Bell-CHSH inequality.** In order to perform a test of the Bell-CHSH inequality³⁹, we send
 312 input photons equally distributed from all states $\{|\pm x\rangle, |\pm y\rangle, |\pm a\rangle, |\pm b\rangle\}$ (Fig. 3b). We select
 313 for cases where two heralding events arise from input photons $\{A, B\} = \pm 1$ that are either 45° or
 314 135° apart from one another. Conditioned on the parity outcome of the BSM (± 1), the Bell-CHSH
 315 inequality bounds the correlations between input photons as

$$S_{\pm} = |\langle A \cdot B \rangle_{xa} - \langle A \cdot B \rangle_{xb} - \langle A \cdot B \rangle_{ya} - \langle A \cdot B \rangle_{yb}| \leq 2, \quad (7)$$

316 where the subscripts denote the bases the photons were sent in. The values of each individual term
 317 in Eq. 7, denoted as “input correlations,” are plotted in Fig. 3d for positive and negative parity
 318 outcomes.

319 **Optimal parameters for asynchronous Bell state measurements.** We minimize the experimen-
 320 tally extracted QBER for the asynchronous BSM to optimize the performance of the memory node.
 321 The first major factor contributing to QBER is the scattering of a third photon that is not detected,
 322 due to the finite heralding efficiency $\eta = 0.423 \pm 0.04$. This is shown in Fig. 2f, where the fidelity
 323 of the spin-photon entangled state diminishes for $\langle n \rangle_m \gtrsim 0.02$. At the same time, we would like
 324 to work at the maximum possible $\langle n \rangle_m$ in order to maximize the data rate to get enough statistics
 325 to extract QBER (and in the quantum communication setting, efficiently generate a key).

326 To increase the key generation rate per channel use, one can also fit many photonic qubits
 327 within each initialization of the memory. In practice, there are 2 physical constraints: (1) the
 328 bandwidth of the SiV-photon interface and (2) the coherence time of the memory. We find that one
 329 can satisfy (1) at a bandwidth of roughly 50 MHz with no measurable infidelity. For shorter optical

330 pulses (< 10 ns), the spin-photon gate fidelity is reduced. In principle, the SiV-photon bandwidth
 331 can be increased by reducing the atom-cavity detuning (here ~ 60 GHz) at the expense of having
 332 to operate at higher magnetic fields where microwave qubit manipulation is not as convenient³⁵.

333 Even with just an XY8-1 decoupling sequence (number of π pulses $N_\pi = 8$), the coherence
 334 time of the SiV is longer than $200 \mu\text{s}$ (Extended Data Fig. 3c) and can be prolonged to the mil-
 335 lisecond range with longer pulse sequences¹⁹. Unfortunately, to satisfy the bandwidth criteria (1)
 336 and to drive both hyperfine transitions (Extended Data Fig. 3a), we must use short (32 ns long π
 337 pulses), which cause additional decoherence from ohmic heating³⁵ already at $N_\pi = 64$ (Extended
 338 Data Fig. 3e). Due to this we limit the pulse sequences to a maximum $N_\pi = 128$, and only use up
 339 to $\approx 20 \mu\text{s}$ of the memory time. One solution would be to switch to superconducting microwave
 340 delivery. Alternatively, one can use a larger value of τ to allow the device to cool down in between
 341 subsequent pulses³⁵ at the expense of having to stabilize a TDI of larger δt . Working at larger δt
 342 also enables temporal multiplexing by fitting multiple time-bin qubits per free-precession interval.
 343 In fact, with $2\tau = 142$ ns, even given constraint (1) and the finite π time, we can already fit up to
 344 4 optical pulses per free-precession window, enabling a total number of photonic qubits of up to
 345 $N = 504$ for only $N_\pi = 128$.

346 In benchmarking the asynchronous BSM for quantum communication, we optimize the pa-
 347 rameters $\langle n \rangle_m$ and N to maximize our enhancement over the direct transmission approach, which
 348 is a combination of both increasing N and reducing the QBER, since a large QBER results in a
 349 small distilled key fraction r_s . As described in the main text, the effective loss can be associated
 350 with $\langle n \rangle_p$, which is the average number of photons per photonic qubit arriving at the device, and

351 is given straightforwardly by $\langle n \rangle_p = \langle n \rangle_m / N$. The most straightforward way to sweep the loss is
 352 to keep the experimental sequence the same (fixed N) and vary the overall power, which changes
 353 $\langle n \rangle_m$. The results of such a sweep are shown in Extended Data Fig. 5a, b. For larger $\langle n \rangle_m$ (cor-
 354 responding to lower effective channel losses), the errors associated with scattering an additional
 355 photon reduce the performance of the memory device.

356 Due to these considerations, we work at roughly $\langle n \rangle_m \lesssim 0.02$ for experiments in the main
 357 text shown in Fig. 3 and 4, below which the performance does not improve significantly. At this
 358 value, we obtain BSM successes at a rate of roughly 0.1 Hz. By fixing $\langle n \rangle_m$ and increasing N , we
 359 maintain a tolerable BSM success rate while increasing the effective channel loss. Eventually, as
 360 demonstrated in Extended Data Fig. 5c and in the high-loss data point in Fig. 4, effects associated
 361 with microwave heating result in errors that again diminish the performance of the memory node
 362 for large N . As such, we conclude that the optimal performance of our node occurs for $\langle n \rangle_m \sim$
 363 0.02 and $N \approx 124$, corresponding to an effective channel loss of 69 dB between Alice and Bob,
 364 which is equivalent to roughly 350 km of telecommunications fiber.

365 We also find that the QBER and thus the performance of the communication link is limited
 366 by imperfect preparation of photonic qubits. Photonic qubits are defined by sending arbitrary phase
 367 patterns generated by the optical AWG to a phase modulator. For an example of such a pattern, see
 368 the blue curve in Fig. 3a. We use an imperfect pulse amplifier with finite bandwidth (0.025 – 700
 369 MHz), and find that the DC component of these waveforms can result in error in photonic qubit
 370 preparation on the few % level. By using a tailored waveform of phases with smaller (or vanishing)
 371 DC component, we can reduce these errors. We run such an experiment during the test of the Bell-

372 CHSH inequality. We find that by evaluating BSM correlations from $|\pm a\rangle$ and $|\pm b\rangle$ inputs during
373 this measurement, we estimate a QBER of 0.097 ± 0.006 .

374 Finally, we obtain the effective clock-rate of the communication link by measuring the total
375 number of photonic qubits sent over the course of an entire experiment. In practice, we record
376 the number of channel uses, determined by the number of sync triggers recorded (see Extended
377 Data Fig. 1a) as well as the number of qubits per sync trigger (N). We then divide this number by
378 the total experimental time from start to finish (~ 1 -2 days for most experimental runs), including
379 all experimental downtime used to stabilize the interferometer, readout and initialize the SiV, and
380 compensate for spectral diffusion and ionization. For $N = 248$, we extract a clock rate of 1.2 MHz.
381 As the distilled key rate in this configuration exceeds the conventional limit of $p/2$ by a factor of
382 3.8 ± 1.1 , it is competitive with a standard linear-optics based system operating at $4.5_{-1.2}^{+1.3}$ MHz
383 clock rate.

384 **Performance of memory-assisted quantum communication.** A single optical link can provide
385 many channels, for example, by making use of different frequency, polarization, or temporal
386 modes. To account for this, when comparing different systems, data rates can be defined on a
387 per-channel-use basis. In a quantum communication setting, full usage of the communication
388 channel between Alice and Bob means that both links from Alice and Bob to Charlie are in use
389 simultaneously. For an asynchronous sequential measurement, typically only half of the channel is
390 used at a time, for example from Alice to Charlie or Bob to Charlie. The other half can in principle
391 be used for a different task when not in use. For example, the unused part of the channel could be
392 routed to a secondary asynchronous BSM device. In our experiment, we can additionally define

393 as a second normalization the rate per channel “occupancy”, which accounts for the fact that only
 394 half the channel is used at any given time. The rate per channel occupancy is therefore half the rate
 395 per full channel use. For comparison, we typically operate at 1.2% channel use and 2.4% channel
 396 occupancy.

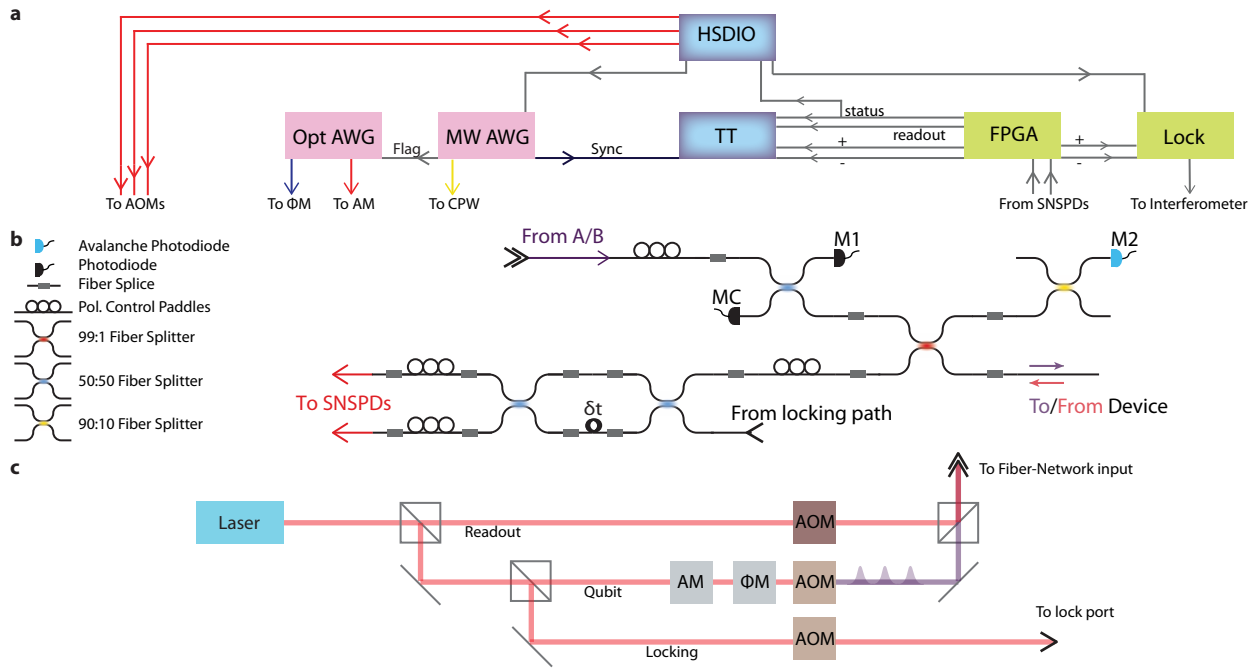
397 To characterize the optimal performance of the asynchronous Bell state measurement device,
 398 we operate it in the optimal regime determined above ($N = 124$, $\langle n \rangle_m \lesssim 0.02$). We note that the
 399 enhancement in the sifted key rate over direct transmission is given by

$$\frac{R}{R_{\max}} = \eta^2 \frac{(N_\pi - 1)(N_\pi - 2)N_{\text{sub}}}{2N_\pi} \quad (8)$$

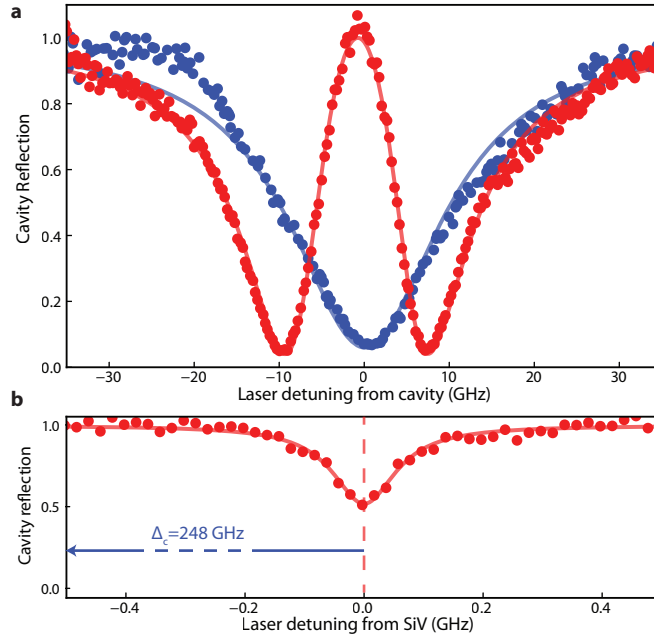
400 and is independent of $\langle n \rangle_m$ for a fixed number of microwave pulses N_π and optical pulses per
 401 microwave pulse N_{sub} and thus fixed $N = N_\pi N_{\text{sub}}$. For low $\langle n \rangle_m$, three photon events become
 402 negligible and therefore QBER saturates, such that the enhancement in the distilled key rate satu-
 403 rates as well (Extended Data Fig. 5a). We can therefore combine all data sets with fixed $N = 124$
 404 below $\langle n \rangle_m \lesssim 0.02$ to characterize the average QBER of 0.116 ± 0.002 (Fig. 3c). The key rates
 405 cited in the main text relate to a data set in this series ($\langle n \rangle_m \approx 0.02$), with a QBER of 0.110 ± 0.004 .
 406 A summary of key rates calculated on a per-channel use and per-channel occupancy basis, as well
 407 as comparisons of performance to an ideal linear-optics BSM and the repeaterless bound⁸ are given
 408 in Extended Data Table 4.

409 Furthermore, we extrapolate the performance of our memory node to include biased input
 410 bases from Alice and Bob. This technique enables a reduction of channel uses where Alice and
 411 Bob send photons in different bases, but is still compatible with secure key distribution²⁶, allowing

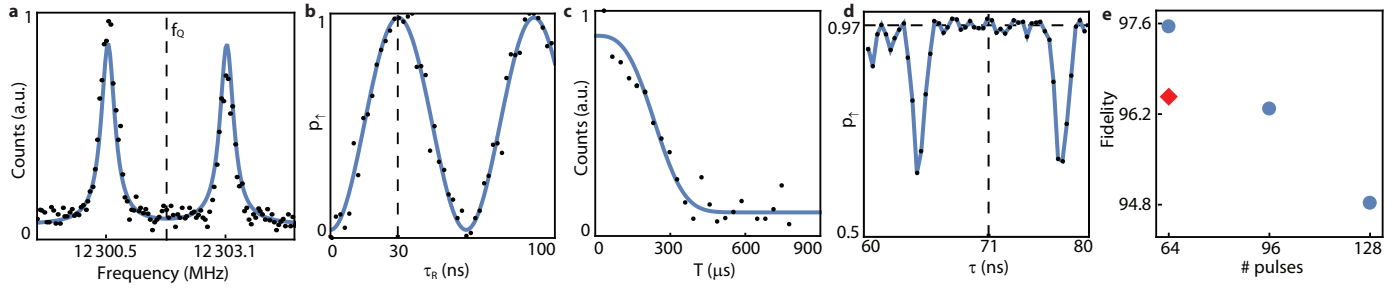
412 for enhanced distilled key rates by at most a factor of 2. The extrapolated performance of our
413 node for a bias of 99:1 is also displayed in Extended Data Table 4, as well as comparisons to the
414 relevant bounds. We note that basis biasing does not affect the performance when comparing to
415 the equivalent direct-transmission experiment, which is limited by $p_{A \rightarrow B}/2$ in the unbiased case
416 and $p_{A \rightarrow B}$ in the biased case. However, using biased input bases does make the performance of the
417 memory-assisted approach more competitive with the fixed repeaterless bound⁸ of $1.44p_{A \rightarrow B}$.



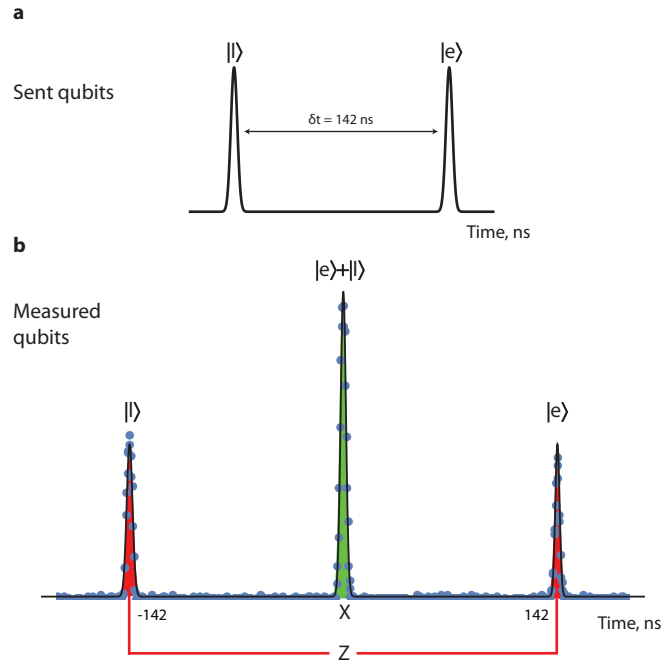
Extended Data Figure 1: Experimental schematic. **a**, Control flow of experiment. Opt (MW) AWG is a Tektronix AWG7122B 5 GS/s (Tektronix AWG70001a 50 GS/s) arbitrary waveform generator used to generate photonic qubits (microwave control signals). All signals are recorded on a time-tagger (TT, PicoQuant HydraHarp 400). **b**, Fiber network used to deliver photons to and collect photons from the memory device, including elements for polarization control and diagnostic measurements of coupling efficiencies. **c**, Preparation of optical fields. The desired phase relation between lock and qubit paths is ensured by modulating AOMs using phase-locked RF sources with a precise 1.8 MHz frequency shift between them.



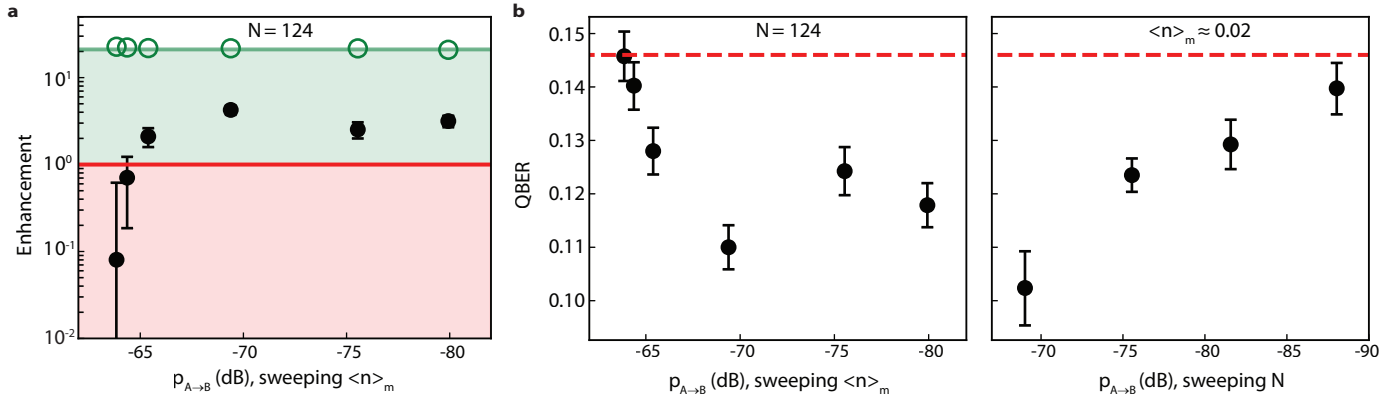
Extended Data Figure 2: Characterization of device cooperativity. **a**, Cavity reflection spectrum far-detuned (blue) and on resonance (red) with SiV center. Blue solid line is a fit to a Lorentzian, enabling extraction of linewidth $\kappa = 21.8$ GHz. Red solid line is a fit to a model used to determine the single-photon Rabi frequency $g = 8.38 \pm 0.05$ GHz and shows the onset of a normal mode splitting. **b**, Measurement of SiV linewidth far detuned ($\Delta_c = 248$ GHz) from cavity resonance. Red solid line is a fit to a Lorentzian, enabling extraction of natural linewidth $\gamma = 0.123$ GHz.



Extended Data Figure 3: Microwave characterization of spin-coherence properties. **a**, ODMR spectrum of the qubit transition at ~ 12 GHz split by coupling to a nearby ^{13}C . **b**, Rabi oscillations showing π time of 30 ns. A π time of 32 ns is used for experiments in the main text. **c**, XY8-1 dynamical decoupling signal (unnormalized) as a function of total time T , showing coherence lasting on the several hundred μs timescale. **d**, XY8-8 dynamical decoupling signal (normalized) revealing region of high fidelity at relevant value of $2\tau = 142$ ns. **e**, Fidelity of spin state after dynamical decoupling sequence with varying number of π pulses (N_π), blue points. Red point (diamond) is under illumination with $\langle n \rangle_m = 0.02$.



Extended Data Figure 4: Measurements on a single time-bin qubit in Z and X bases. **a**, Example of optical pulses sent for example in the experiment described in Fig. 2d. **b**, Time trace of detected photons on + detector when pulses shown in (a) are sent directly into the TDI. The first and last peaks correspond to late and early photons taking the long and short paths of the TDI, which enable measurements in the Z basis $\{|e\rangle, |l\rangle\}$. The central bin corresponds to the late and early components overlapping and interfering constructively to come out of the + port, equivalent to a measurement of the time bin qubit in the $|+x\rangle$ state. A detection event in this same timing window on the - detector (not shown) would constitute a $| -x\rangle$ measurement. In this measurement, the TDI was left unlocked, so we observe no interference in the central window.



Extended Data Figure 5: Performance of memory-device versus of channel loss. **a**, Enhancement of memory-based approach compared to direct transmission approach, keeping $N = 124$ fixed and varying $\langle n \rangle_m$ in order to vary the effective channel transmission probability $p_{A \rightarrow B}$. At high $p_{A \rightarrow B}$ (larger $\langle n \rangle_m$), r_s approaches 0 due to increased QBER arising from undetected scattering of a third photon. **b**, (Left) Plot of QBER for same sweep of $\langle n \rangle_m$ shown in **a**. (Right) Plot of QBER while sweeping N in order to vary loss. These points correspond to the same data shown in Fig. 4. At lower $p_{A \rightarrow B}$ (larger N), microwave-induced heating-related dephasing leads to increased QBER.

Step	Process	Duration	Proceed to
1	Lock time-delay interferometer	200 ms	2
2	Readout SiV	30 μ s	If status LOW: 4, else: 3
3	Apply microwave π pulse	32 ns	2
4	Run main experiment script	\sim 200 ms	1

Extended Data Table 1: High-level experimental sequence. This sequence is programmed into the HSDIO and uses feedback from the status trigger sent from the FPGA (see Extended Data Fig. 1a). Main experimental sequence is described in Extended Data Table 2. External software is also used to monitor the status trigger. If it is HI for \gtrsim 2 s, the software activates an automatic re-lock procedure which compensates for spectral diffusion and ionization of the SiV center (Methods).

Step	Process	Duration	Proceed to
1	Run sequence in Fig. 3a for a given N	$10 - 20 \mu\text{s}$	2
2	Readout SiV + report readout to TT	$30 \mu\text{s}$	If status LOW: 1, else: 3
3	Apply microwave π pulse	32 ns	4
4	Readout SiV	$30 \mu\text{s}$	If status LOW: 3, else: 1

Extended Data Table 2: Main experimental sequence for memory-enhanced quantum communication. This script is followed until step 1 is run a total of 4000 times, and then terminates and returns to step 1 of Extended Data Table 1. The longest step is the readout step, which is limited by the fact that we operate at a photon detection rate of $\sim 1 \text{ MHz}$ to avoid saturation of the SNSPDs.

Alice	Bob	Parity	Bell state
$ +x\rangle$	$ +x\rangle$	+1	$ \Phi_+\rangle$
$ +x\rangle$	$ -x\rangle$	-1	$ \Phi_-\rangle$
$ -x\rangle$	$ +x\rangle$	-1	$ \Phi_-\rangle$
$ -x\rangle$	$ -x\rangle$	+1	$ \Phi_+\rangle$
$ +y\rangle$	$ +y\rangle$	-1	$ \Phi_-\rangle$
$ +y\rangle$	$ -y\rangle$	+1	$ \Phi_+\rangle$
$ -y\rangle$	$ +y\rangle$	+1	$ \Phi_+\rangle$
$ -y\rangle$	$ -y\rangle$	-1	$ \Phi_-\rangle$

Extended Data Table 3: Truth table of asynchronous BSM protocol, showing the parity (and BSM outcome) for each set of valid input states from Alice and Bob. In the case of Y basis inputs, Alice and Bob adjust the sign of their input state depending on whether it was commensurate with an even or odd numbered free-precession interval, based on timing information provided by Charlie (Methods).

	per channel occupancy	per channel occupancy	per channel use	per channel use
X:Y basis bias	50 : 50	99 : 1	50 : 50	99 : 1
Distilled key rate R [10^{-7}]	$1.19^{+0.14}_{-0.14}$	$2.33^{+0.28}_{-0.28}$	$2.37^{+0.29}_{-0.28}$	$4.66^{+0.56}_{-0.55}$
$R/R_{\max}(\mathbf{X}:\mathbf{Y})$	$2.06^{+0.25}_{-0.25}$	$2.06^{+0.25}_{-0.25}$	$4.13^{+0.50}_{-0.49}$	$4.13^{+0.50}_{-0.49}$
$R/(1.44p_{A \rightarrow B})$	$0.71^{+0.09}_{-0.08}$	$1.40^{+0.17}_{-0.17}$	$1.43^{+0.17}_{-0.17}$	$2.80^{+0.34}_{-0.33}$
1–confidence level		$1.1^{+0.4}_{-0.3} \times 10^{-2}$	$8^{+3}_{-2} \times 10^{-3}$	$1.3^{+0.5}_{-0.3} \times 10^{-7}$

Extended Data Table 4: Quantum-memory-based advantage. Distilled key rates with the asynchronous BSM device and comparison to ideal direct communication implementations, based on the performance of our network node for $N = 124$ and $\langle n \rangle_m \sim 0.02$. Distillable key rates for $E = 0.110 \pm 0.004$ for unbiased and biased basis choice are expressed in a per-channel-occupancy and per-channel-use normalization (Methods). Enhancement is calculated versus the linear optics BSM limit ($R_{\max}(50 : 50) = p_{A \rightarrow B}/2$ for unbiased bases, $R_{\max}(99 : 1) = 0.98p_{A \rightarrow B}$ with biased bases) and versus the fundamental repeaterless channel capacity⁸ ($1.44p_{A \rightarrow B}$). Confidence levels for surpassing the latter bound⁸ are given in the final row.

- 418 1. Kimble, H. J. The quantum internet. *Nature* **453**, 1023 (2008). URL
420 <https://doi.org/10.1038/nature07127>.
- 421 2. Bennett, C. H. & Brassard, G. Quantum cryptography: Public key dis-
422 tribution and coin tossing. *Proceedings of the IEEE International Confer-*
423 *ence on Computers, Systems and Signal Processing* **175**, 8 (1984). URL
424 <https://doi.org/10.1016/j.tcs.2014.05.025>.
- 425 3. Shor, P. W. & Preskill, J. Simple proof of security of the BB84 quantum
426 key distribution protocol. *Physical Review Letters* **85**, 441–444 (2000). URL
427 <https://doi.org/10.1103/PhysRevLett.85.441>.
- 428 4. Gisin, N., Ribordy, G., Tittel, W. & Zbinden, H. Quantum cryp-
429 tography. *Reviews of Modern Physics* **74**, 145–195 (2002). URL
430 <https://doi.org/10.1103/RevModPhys.74.145>.
- 431 5. Boaron, A. *et al.* Secure Quantum Key Distribution over 421 km
432 of Optical Fiber. *Physical Review Letters* **121**, 1–4 (2018). URL
433 <https://doi.org/10.1103/PhysRevLett.121.190502>.
- 434 6. Zhang, Q., Xu, F., Chen, Y.-A., Peng, C.-Z. & Pan, J.-W. Large scale quantum key distri-
435 bution: challenges and solutions [Invited]. *Optics Express* **26**, 24260–24273 (2018). URL
436 <https://doi.org/10.1364/OE.26.024260>.
- 437 7. Pirandola, S. *et al.* Advances in Quantum Cryptography (2019). URL
438 <http://arxiv.org/abs/1906.01645>.

- 439 8. Pirandola, S., Laurenza, R., Ottaviani, C. & Banchi, L. Fundamental limits of re-
440 peaterless quantum communications. *Nature Communications* **8**, 15043 (2017). URL
441 <https://doi.org/10.1038/ncomms15043>.
- 442 9. Briegel, H.-J., Dür, W., Cirac, J. I. & Zoller, P. Quantum Repeaters: The Role of Imperfect Lo-
443 cal Operations in Quantum Communication. *Physical Review Letters* **81**, 5932–5935 (1998).
444 URL <https://doi.org/10.1103/PhysRevLett.81.5932>.
- 445 10. Chou, C.-W. *et al.* Functional Quantum Nodes for Entanglement Distribution over
446 Scalable Quantum Networks. *Science* **316**, 1316 LP – 1320 (2007). URL
447 <https://doi.org/10.1126/science.1140300>.
- 448 11. Yuan, Z.-S. *et al.* Experimental demonstration of a BDCZ quantum repeater node. *Nature*
449 **454**, 1098 (2008). URL <https://doi.org/10.1038/nature07241>.
- 450 12. Gao, W. B., Fallahi, P., Togan, E., Miguel-Sanchez, J. & Imamoglu, A. Observation of en-
451 tanglement between a quantum dot spin and a single photon. *Nature* **491**, 426 (2012). URL
452 <https://doi.org/10.1038/nature11573>.
- 453 13. Reiserer, A. & Rempe, G. Cavity-based quantum networks with single atoms
454 and optical photons. *Reviews of Modern Physics* **87**, 1379–1418 (2015). URL
455 <https://doi.org/10.1103/RevModPhys.87.1379>.
- 456 14. Hensen, B. *et al.* Loophole-free Bell inequality violation using elec-
457 tron spins separated by 1.3 kilometres. *Nature* **526**, 682 (2015). URL
458 <https://doi.org/10.1038/nature15759>.

- 459 15. Kalb, N. *et al.* Entanglement distillation between solid-state quantum network nodes. *Science*
460 **356**, 928 LP – 932 (2017). URL <https://doi.org/10.1126/science.aan0070>.
- 461 16. Kaneda, F., Xu, F., Chapman, J. & Kwiat, P. G. Quantum-memory-assisted multi-photon
462 generation for efficient quantum information processing. *Optica* **4**, 1034–1037 (2017). URL
463 <https://doi.org/10.0.5.84/OPTICA.4.001034>.
- 464 17. Evans, R. E. *et al.* Photon-mediated interactions between quantum emit-
465 ters in a diamond nanocavity. *Science* **362**, 662 LP – 665 (2018). URL
466 <https://doi.org/10.1126/science.aau4691>.
- 467 18. Burek, M. J. *et al.* Fiber-Coupled Diamond Quantum Nanopho-
468 tonic Interface. *Physical Review Applied* **8**, 24026 (2017). URL
469 <https://doi.org/10.1103/PhysRevApplied.8.024026>.
- 470 19. Nguyen, C. T. *et al.* Quantum Network Nodes Based on Diamond Qubits with
471 an Efficient Nanophotonic Interface. *Phys. Rev. Lett.* **123**, 183602 (2019). URL
472 <https://link.aps.org/doi/10.1103/PhysRevLett.123.183602>.
- 473 20. Monroe, C. *et al.* Large-scale modular quantum-computer architecture with atomic
474 memory and photonic interconnects. *Physical Review A* **89**, 22317 (2014). URL
475 <https://doi.org/10.1103/PhysRevA.89.022317>.
- 476 21. Lo, H.-K., Curty, M. & Qi, B. Measurement-Device-Independent Quan-
477 tum Key Distribution. *Physical Review Letters* **108**, 130503 (2012). URL
478 <https://doi.org/10.1103/PhysRevLett.108.130503>.

- 479 22. Braunstein, S. L. & Pirandola, S. Side-Channel-Free Quantum Key
480 Distribution. *Physical Review Letters* **108**, 130502 (2012). URL
481 <https://doi.org/10.1103/PhysRevLett.108.130502>.
- 482 23. Minder, M. *et al.* Experimental quantum key distribution beyond the re-
483 peaterless secret key capacity. *Nature Photonics* **13**, 334–338 (2019). URL
484 <https://doi.org/10.1038/s41566-019-0377-7>.
- 485 24. Panayi, C., Razavi, M., Ma, X. & Lütkenhaus, N. Memory-assisted measurement-device-
486 independent quantum key distribution. *New Journal of Physics* **16**, 43005 (2014). URL
487 <https://doi.org/10.1088/1367-2630/16/4/043005>.
- 488 25. Lo, H.-K., Ma, X. & Chen, K. Decoy State Quantum Key Dis-
489 tribution. *Physical Review Letters* **94**, 230504 (2005). URL
490 <https://link.aps.org/doi/10.1103/PhysRevLett.94.230504>.
- 491 26. Lo, H.-K., Chau, H. F. & Ardehali, M. Efficient Quantum Key Distribution Scheme and
492 a Proof of Its Unconditional Security. *Journal of Cryptology* **18**, 133–165 (2005). URL
493 <https://doi.org/10.1007/s00145-004-0142-y>.
- 494 27. Curty, M. *et al.* Finite-key analysis for measurement-device-independent
495 quantum key distribution. *Nature Communications* **5**, 3732 (2014). URL
496 <https://doi.org/10.1038/ncomms4732>.

- 497 28. Duan, L.-M. & Kimble, H. J. Scalable Photonic Quantum Computation through
498 Cavity-Assisted Interactions. *Physical Review Letters* **92**, 127902 (2004). URL
499 <https://link.aps.org/doi/10.1103/PhysRevLett.92.127902>.
- 500 29. Biham, E., Huttner, B. & Mor, T. Quantum cryptographic network based
501 on quantum memories. *Physical Review A* **54**, 2651–2658 (1996). URL
502 <https://link.aps.org/doi/10.1103/PhysRevA.54.2651>.
- 503 30. Machielse, B. *et al.* Quantum Interference of Electromechanically Stabilized Emit-
504 ters in Nanophotonic Devices. *Physical Review X* **9**, 31022 (2019). URL
505 <https://link.aps.org/doi/10.1103/PhysRevX.9.031022>.
- 506 31. Raussendorf, R. & Briegel, H. J. A One-Way Quantum Com-
507 puter. *Physical Review Letters* **86**, 5188–5191 (2001). URL
508 <https://link.aps.org/doi/10.1103/PhysRevLett.86.5188>.
- 509 32. Borregaard, J. *et al.* One-way quantum repeater based on near-deterministic photon-emitter
510 interfaces 1–19 (2019). URL <http://arxiv.org/abs/1907.05101>.
- 511 33. Burek, M. J. *et al.* High quality-factor optical nanocavities in bulk
512 single-crystal diamond. *Nature Communications* **5**, 5718 (2014). URL
513 <https://doi.org/10.1038/ncomms6718>.
- 514 34. Atikian, H. A. *et al.* Freestanding nanostructures via reactive ion beam angled etching. *APL*
515 *Photonics* **2**, 51301 (2017). URL <https://doi.org/10.1063/1.4982603>.

- 516 35. Nguyen, C. T. *et al.* An integrated nanophotonic quantum register based on
517 silicon-vacancy spins in diamond. *Phys. Rev. B* **100**, 165428 (2019). URL
518 <https://link.aps.org/doi/10.1103/PhysRevB.100.165428>.
- 519 36. de Riedmatten, H. *et al.* Tailoring photonic entanglement in high-
520 dimensional Hilbert spaces. *Physical Review A* **69**, 50304 (2004). URL
521 <https://doi.org/10.1103/PhysRevA.69.050304>.
- 522 37. Sasaki, T., Yamamoto, Y. & Koashi, M. Practical quantum key distribution pro-
523 tocol without monitoring signal disturbance. *Nature* **509**, 475 (2014). URL
524 <https://doi.org/10.1038/nature13303>.
- 525 38. Kalb, N., Reiserer, A., Ritter, S. & Rempe, G. Heralded Storage of a Photonic
526 Quantum Bit in a Single Atom. *Physical Review Letters* **114**, 220501 (2015). URL
527 <https://doi.org/10.1103/PhysRevLett.114.220501>.
- 528 39. Clauser, J. F., Horne, M. A., Shimony, A. & Holt, R. A. Proposed Experiment to Test
529 Local Hidden-Variable Theories. *Physical Review Letters* **23**, 880–884 (1969). URL
530 <https://doi.org/10.1103/PhysRevLett.23.880>.

531 **Acknowledgements** We thank Pavel Stroganov, Kristiaan de Greve, Johannes Borregaard, Eric Bersin,
532 Benjamin Dixon, and Neil Sinclair for discussions, Vikas Anant from PhotonSpot for providing SNSPDs,
533 and Jim MacArthur for assistance with electronics. This work was supported by the NSF, CUA, DoD/ARO
534 DURIP, AFOSR MURI, ONR MURI, ARL, and a Vannevar Bush Faculty Fellowship. Devices were fab-
535 ricated at Harvard CNS, NSF award no. 1541959. M. K. B. and D. S. L. acknowledge support from an

536 NDSEG Fellowship. R. R. acknowledges support from the Alexander von Humbolt Foundation. B. M. and
537 E. N. K. acknowledge support from an NSF GRFP.

538 **Competing Interests** The authors declare that they have no competing financial interests.

539 **Correspondence** Correspondence and requests for materials should be addressed to M. D. L. at

540 lukin@physics.harvard.edu